Molecular Organization of Crystalline β–Carotene in Carrots Determined with Polarization-Dependent Second and Third Harmonic Generation Microscopy

6 AUTHORS, INCLUDING:

Danielle Tokarz
University of Toronto
20 PUBLICATIONS   **73** CITATIONS

SEE PROFILE

Richard Cisek
University of Toronto
49 PUBLICATIONS   **445** CITATIONS

SEE PROFILE

Serguei Krouglov
University of Toronto
175 PUBLICATIONS   **471** CITATIONS

SEE PROFILE

Ulrich Fekl
University of Toronto
51 PUBLICATIONS   **887** CITATIONS

SEE PROFILE

Molecular Organization of Crystalline β-Carotene in Carrots Determined with Polarization-Dependent Second and Third Harmonic Generation Microscopy

Danielle Tokarz,[†,‡] Richard Cisek,[†,§] Serguei Krouglov,[†,§] Lukas Kontenis,[†,§] Ulrich Fekl,[†,‡] and Virginijus Barzda*[,†,‡,§]

[†]Department of Chemical and Physical Sciences, University of Toronto Mississauga, 3359 Mississauga Road North, Mississauga, Ontario, Canada L5L 1C6

[‡]Department of Chemistry, University of Toronto, 80 St. George Street, Toronto, Ontario, Canada M5S 3H6

[§]Department of Physics and Institute for Optical Sciences, University of Toronto, 60 St. George Street, Toronto, Ontario, Canada M5S 1A7

S Supporting Information

ABSTRACT: Polarization-in, polarization-out (PIPO) second harmonic generation (SHG) and third harmonic generation (THG) microscopy was used to study the crystalline organization of β-carotene molecules within individual aggregates contained in the chromoplasts of orange carrots *in vivo*. Multimodal PIPO SHG and PIPO THG studies of the aggregates revealed one dominant SHG and THG dipole signifying that β-carotene molecules are oriented along a single axis. Three-dimensional visualization of the orientation of β-carotene molecules with respect to the aggregate axis was also performed with both microscopy modalities and revealed organization of the aggregates as ribbon-like structures consisting of twists and folds. Therefore, PIPO SHG and PIPO THG microscopy provides information on the crystalline organization and the orientation of ordered biological structures *in vivo* where multimodal polarization dependent SHG and THG investigations are particularly advantageous as both noncentrosymmetric and centrosymmetric crystalline organizations can be probed.
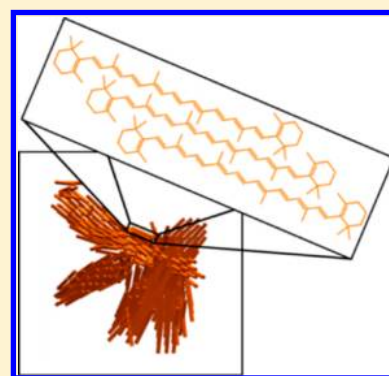
■ INTRODUCTION

The investigation of self-assembled molecular aggregates links studies between single molecules and structurally ordered crystals. Molecular aggregates can be formed due to hydrogen bonding, dipole forces, and van der Waals interactions.[1] In particular, carotenoids are well-known to crystallize when dissolved in hydrated polar solvents,[2−6] and also to assemble to form aggregates *in vivo*. For instance, within the chromoplasts of carrots and *Narcissus* flowers, the concentration of β-carotene can be so high that β-carotene crystallizes.[1] Similarly, in red tomatoes, large crystals of lycopene form in the chromoplasts.[1] Crystallization of carotenoids occurs inside the lumen of thylakoids, and therefore the β-carotene or lycopene crystals remain enveloped by a membrane.[1] Chromoplasts have been found to range in structure from globular, tubular, reticulo-tubular, membranous, and crystalline types;[7] however, it is difficult to evaluate the structure of aggregates present in chromoplasts since a variety of carotenoid aggregates may exist in the same chromoplast,[1] and thus each chromoplast has to be investigated individually.

Little research has concentrated on the ultrastructure of β-carotene within the chromoplasts of orange carrots. Previous research has studied the structure of β-carotene crystals within chromoplasts by electron microscopy.[7−11] Electron microscopy studies revealed ribbon-like structures of β-carotene aggregates

in chromoplasts. Recently, Brackmann et al. studied β-carotene aggregates in carrots, sweet potatoes, and mangos with second harmonic generation (SHG) microscopy.[12] They identified different sizes and shapes of β-carotene crystals and aggregates *in vivo*.[12] As will be shown in this paper, β-carotene crystals give rise to both SHG and THG signal; therefore, both nonlinear optical microscopy techniques can be used to identify β-carotene crystals. In addition, carotenoid aggregates with a certain order or crystalline organization will exhibit polarization dependent nonlinear SHG and THG signals, which can be used to elucidate organization of molecules in the aggregates. In order to perform polarization-dependent SHG and THG experiments, SHG and THG intensities are measured while the orientation of the incident laser polarization is varied. Laser polarization-dependent SHG has been previously used for quantifying organizational changes in collagen,[13−21] muscle,[21−27] microtubules of neurons,[28,29] starch,[30−32] and other proteins such as phenylalanine hydroxylase from *Chromobacterium violaceum*.[33] Laser polarization-dependent THG has also been applied to study muscle,[23] cornea,[34] and skin.[35] In order to gain further insight, an analyzer was added to

investigate the polarization of generated second and third harmonic radiation. This technique is referred to as polarization-in, polarization-out (PIPO) harmonic generation microscopy.[36] Since the symmetry of a crystalline structure is reflected in the symmetry of the nonlinear optical susceptibility tensor, PIPO harmonic generation microscopy can be used to investigate the crystallographic structure and the orientation of the crystalline aggregates in microscopic samples. PIPO SHG microscopy has been applied to study the second-order nonlinear optical susceptibility ratio $(\chi^{(2)}_{ZZZ}{}'/\chi^{(2)}_{ZXX}{}')$ and the average fibril orientation of fibrillar collagen in various tissues,[36,37] while the application of PIPO THG microscopy will be demonstrated in this article for the first time. The development of a polarization-dependent THG technique to study structure is particularly important because THG often gives contrast to different structures than SHG, and therefore carries complementary information about the structural organization of crystalline aggregates. This research shows that structural studies using optical measurements can be performed *in vivo*, which is important for noninvasive biomedical investigations.

■ THEORETICAL METHODS

Second-Order Nonlinear Optical Susceptibility Tensor of an Arbitrarily Oriented Cylinder. The nonlinear optical susceptibility tensor of an arbitrarily oriented crystal structure that contains cylindrically symmetric molecules is described within the laboratory frame of reference using Cartesian coordinates, XYZ. The orientation of the cylindrical axis can be defined in the extrinsic laboratory frame with modified spherical coordinates, α and δ. The angle, α, is between the axis of the cylinder and its projection in the XZ plane while the orientation angle, δ, of the cylinder in the projection plane is defined between the laboratory frame axis Z and the projection of the cylinder axis onto the XZ plane. The cylinder itself is associated with its own Cartesian coordinates, xyz, where the z-axis is oriented along the cylindrical axis. In a nonlinear microscopy image, the cylinder appears projected onto the XZ plane. Therefore, it is convenient to introduce an additional laboratory coordinate system, $X'Y'Z'$, which is rotated by the angle δ from the Z-axis, and therefore, the Z'-axis appears oriented along the projection of the z-axis onto the XZ plane.

The second-order nonlinear optical susceptibility tensor components $(\chi^{(2)}_{IJK})$ in the laboratory frame can be related to the second-order nonlinear optical susceptibility tensor of the cylinder $(\chi^{(2)}_{ijk})$ rotated by angles, α and δ. The I, J, K indexes represent the laboratory frame of reference, while indexes i, j, k are associated with the reference frame of the cylinder. If it is assumed that one dominant nonlinear dipole exists in the z direction along the axis of the cylindrical structure, then all other tensor components are small and it can be assumed that $\chi^{(2)}_{zxx} = \chi^{(2)}_{xzx} = \chi^{(2)}_{xxz}$.[38] With this assumption, the second-order nonlinear optical susceptibility tensor components of the sample are expressed as follows:[37]

$$\chi^{(2)}_{ZZZ} = \cos\alpha\cos\delta[(\chi^{(2)}_{zzz}/\chi^{(2)}_{zxx} - 3)\cos^2\alpha\cos^2\delta + 3]\chi^{(2)}_{zxx} \tag{1}$$

$$\chi^{(2)}_{ZXX} = \cos\alpha\cos\delta[(\chi^{(2)}_{zzz}/\chi^{(2)}_{zxx} - 3)\cos^2\alpha\sin^2\delta + 1]\chi^{(2)}_{zxx} \tag{2}$$

$$\chi^{(2)}_{XZZ} = \cos\alpha\sin\delta[(\chi^{(2)}_{zzz}/\chi^{(2)}_{zxx} - 3)\cos^2\alpha\cos^2\delta + 1]\chi^{(2)}_{zxx} \tag{3}$$

$$\chi^{(2)}_{XXX} = \cos\alpha\sin\delta[(\chi^{(2)}_{zzz}/\chi^{(2)}_{zxx} - 3)\cos^2\alpha\sin^2\delta + 3]\chi^{(2)}_{zxx} \tag{4}$$

In order to identify the orientation of the cylinder axes within a focal volume, the second-order nonlinear optical susceptibility tensor component ratios are determined from PIPO second harmonic generation measurements.[37] A general SHG intensity equation for PIPO measurements was derived:[37]

$$I_{2\omega} \propto \left| \sin\varphi' \left(\frac{\chi^{(2)}_{XXX}{}'}{\chi^{(2)}_{ZXX}{}'}\sin^2\theta' + \sin 2\theta' + \frac{\chi^{(2)}_{XZZ}{}'}{\chi^{(2)}_{ZXX}{}'}\cos^2\theta' \right) \right.$$
$$\left. + \cos\varphi'\left(\sin^2\theta' + \frac{\chi^{(2)}_{XZZ}{}'}{\chi^{(2)}_{ZXX}{}'}\sin 2\theta' + \frac{\chi^{(2)}_{ZZZ}{}'}{\chi^{(2)}_{ZXX}{}'}\cos^2\theta' \right) \right|^2 \tag{5}$$

where θ' is the angle between the incident polarization and the laboratory Z'-axis, while ϕ' is the angle between the analyzer and the Z'-axis, within the XZ plane. The prime signifies that the susceptibility values and the polarizer and analyzer angles are obtained for the $X'Y'Z'$ coordinate system. The $\theta' = \theta - \delta$ and $\phi' = \phi - \delta$; therefore, when $\delta = 0$ the $X'Y'Z'$ coordinate system coincides with XYZ laboratory coordinate system.

Third-Order Nonlinear Optical Susceptibility Tensor of an Arbitrarily Oriented Cylinder. Similarly, the third-order nonlinear optical susceptibility tensor components $(\chi^{(3)}_{IJKL})$ of an arbitrarily oriented cylinder are related to the third-order nonlinear optical susceptibility tensor $(\chi^{(3)}_{ijkl})$ of the cylinder rotated by angles, α and δ, as well as related to the $\chi^{(3)}_{IJKL}{}'$ tensor rotated by δ from the Z-axis. If it is assumed that one dominant nonlinear dipole exists along the z-axis of the cylinder, then all other tensor components are small. Analogous to SHG, it is assumed that $\chi^{(3)}_{zzxx} = \chi^{(3)}_{xxzz} = \chi^{(3)}_{xzzx} = \chi^{(3)}_{zxxz} = \chi^{(3)}_{zxzx} = \chi^{(3)}_{xzxz}$. With this assumption, the third-order nonlinear optical susceptibility tensor components of a cylindrical structure are expressed as follows:

$$\chi^{(3)}_{ZZZZ} = \chi^{(3)}_{xxxx} - 2(\chi^{(3)}_{xxxx} - 3\chi^{(3)}_{zzxx})\cos^2\alpha\cos^2\delta$$
$$+ (\chi^{(3)}_{xxxx} - 6\chi^{(3)}_{zzxx} + \chi^{(3)}_{zzzz})\cos^4\alpha\cos^4\delta \tag{6}$$

$$\chi^{(3)}_{ZZXX} = \frac{1}{3}\chi^{(3)}_{xxxx} + \left(\chi^{(3)}_{zzxx} - \frac{1}{3}\chi^{(3)}_{xxxx}\right)\cos^2\alpha$$
$$+ [\chi^{(3)}_{xxxx} - 6\chi^{(3)}_{zzxx} + \chi^{(3)}_{zzzz} + (6\chi^{(3)}_{zzxx} - \chi^{(3)}_{xxxx}$$
$$- \chi^{(3)}_{zzzz})\cos^2\delta]\cos^4\alpha\cos^2\delta \tag{7}$$

$$\chi^{(3)}_{XXXX} = \chi^{(3)}_{xxxx} + 2(3\chi^{(3)}_{zzxx} - \chi^{(3)}_{xxxx})\sin^2\delta$$
$$+ (\chi^{(3)}_{xxxx} - 6\chi^{(3)}_{zzxx} + \chi^{(3)}_{zzzz})\sin^4\delta$$
$$+ 2(\chi^{(3)}_{xxxx} - 3\chi^{(3)}_{zzxx})\sin^2\alpha\sin^2\delta$$
$$+ 2(6\chi^{(3)}_{zzxx} - \chi^{(3)}_{xxxx} - \chi^{(3)}_{zzzz})\sin^2\alpha\sin^4\delta$$
$$+ (\chi^{(3)}_{xxxx} - 6\chi^{(3)}_{zzxx} + \chi^{(3)}_{zzzz})\sin^4\alpha\sin^4\delta \tag{8}$$

The third-order nonlinear optical susceptibility tensor component ratios deduced from PIPO third harmonic generation measurements are expressed by a general THG intensity equation which was derived analogous to Tuer et al.:[37]
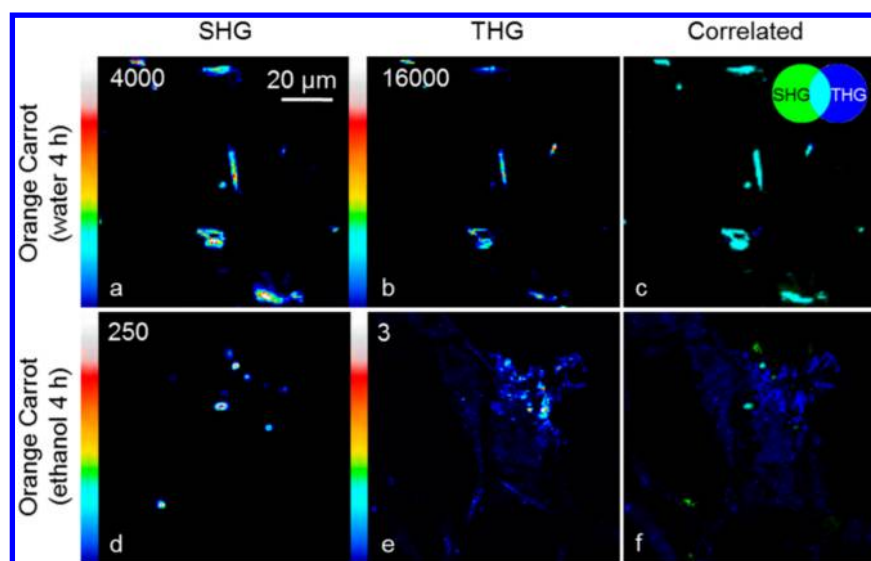
Figure 1. SHG and THG images of orange carrot immersed in water and ethanol: (a) SHG, (b) THG, and (c) the correlated image of carrot contained in water for 4 h; (d) SHG, (e) THG, and (f) the correlated image of carrot contained in ethanol for 4 h. The image intensities shown on the top left of SHG and THG images are scaled to one another. In the structural cross-correlation image analysis, uncorrelated SHG signal is colored green, uncorrelated THG signal is colored blue, and the correlated SHG and THG signals are colored cyan. The color scheme is shown in the top right corner of image (c).

$$
\begin{aligned}
I_{3\omega} \propto \frac{(\chi^{(3)}_{XXXX}{}')^2}{16} \Bigg| & \sin\varphi'\sin\theta'\left(\frac{\cos^2\theta'(3\chi^{(3)}_{ZZXX}{}' - \chi^{(3)}_{XXXX}{}')}{\chi^{(3)}_{XXXX}{}'} + 1\right) \\
& + \cos\varphi'\cos\theta'\left(\left(\frac{3\chi^{(3)}_{ZZXX}{}'}{\chi^{(3)}_{XXXX}{}'}\right) - \cos^2\theta'\left(\frac{2\chi^{(3)}_{ZZXX}{}' - \chi^{(3)}_{ZZZZ}{}'}{\chi^{(3)}_{XXXX}{}'}\right)\right)\Bigg|^2
\end{aligned}
\tag{9}
$$

where the prime signifies that values are used in the $X'Y'Z'$ coordinate system.

EXPERIMENTAL METHODS

Carrot Sample Preparation. Fresh orange carrot root (*Daucus carota*) was obtained at the local market and stored at 20 °C. In order to visualize crystalline β-carotene aggregates within the tissue, thin slices from fresh orange carrot were sectioned longitudinally with respect to the root axes and placed onto glass coverslips. The carrot slices were immersed in either water or ethanol for microscopy studies as indicated in the Results section. A second coverslip was used to cover the carrot tissue sections.

Chromoplast Isolation. The chromoplast isolation followed a similar procedure for chloroplast isolation.[39] About 60 g of fresh orange carrot was homogenized in a buffer containing 20 mM Tricene, 0.35 M Sorbitol, and 0.2 mM $MgCl_2$ at pH 7.8. The suspension was filtered through 8 layers of cheesecloth and centrifuged for 15 s at 2000 g. The supernatant was removed and centrifuged for 3 min at 4000 g. The remaining pellet was washed with 0.35 M Sorbitol and 1 mM Tricene at pH 7.8 and again centrifuged at 4000 g for 4 min. The pellet was then suspended in a buffer solution containing 0.35 M Sorbitol, 20 mM Tricine, 5 mM $MgCl_2$, and 10 mM KCl. The UV–Vis absorption of the fresh chromoplast suspension was recorded with an Olis-14 (upgraded Cary-14) spectrophotometer using a 1 cm Suprasil quartz cuvette (Hellma). Fresh chromoplasts were used for imaging.

Nonlinear Optical Microscope Setup. The laser source consisted of a femtosecond Yb:KGd(WO$_4$)$_2$ oscillator, which provided ~450 fs duration pulses at a wavelength of 1028 nm with a pulse repetition rate of 14.3 MHz.[40] The laser was coupled into a home-built laser scanning microscope described elsewhere.[41] A high numerical aperture (NA) air objective (20× 0.75 NA, Zeiss) was used for imaging. PIPO SHG and PIPO THG measurements were performed sequentially, one after the other. SHG and THG signal was collected in the forward direction through a home-built UV transmitting objective and filtered with a band-pass interference filter (F10−514.5, CVI Melles Griot) and a color glass filter (BG-39, CVI Melles Griot) for SHG and F10−340 (CVI Melles Griot) for THG. The signals were measured using photon-counting detectors (SHG: H7421−40, Hamamatsu, and THG: MP−1343, Perkin-Elmer).

Polarization-in, Polarization-Out (PIPO) Measurements. A multicontrast nonlinear optical microscope was modified for PIPO measurements as previously described.[36,37] Briefly, a linear polarizer (IR 1100 BC4, Laser Components Inc.) and a half-wave plate (custom flat, Comar) were inserted before the excitation objective. The analyzer, a linear polarizer for the visible region (10LP-VIS-B, Newport), was placed after the collection objective for determination of the SHG polarization, while a linear polarizer for the UV region (10LP-UV, Newport) was placed after the collection objective for determination of the THG polarization.

SHG and THG images were collected at 132 sets of excitation and analyzer angles. The half-wave plate was rotated to 11 different polarization orientations evenly spaced between excitation angles from $-\pi/2$ to $\pi/2$, whereas the analyzer was rotated to 11 different evenly spaced polarization orientation angles from $-\pi/2$ to $\pi/2$ for each excitation polarization angle. Reference frames to monitor fluctuations in SHG and THG intensity due to sample photobleaching were imaged every 11 measurements.

For each 2×2 pixel area, the variation in SHG and THG intensity as a function of θ and φ was fit using eq 5 for SHG

3816

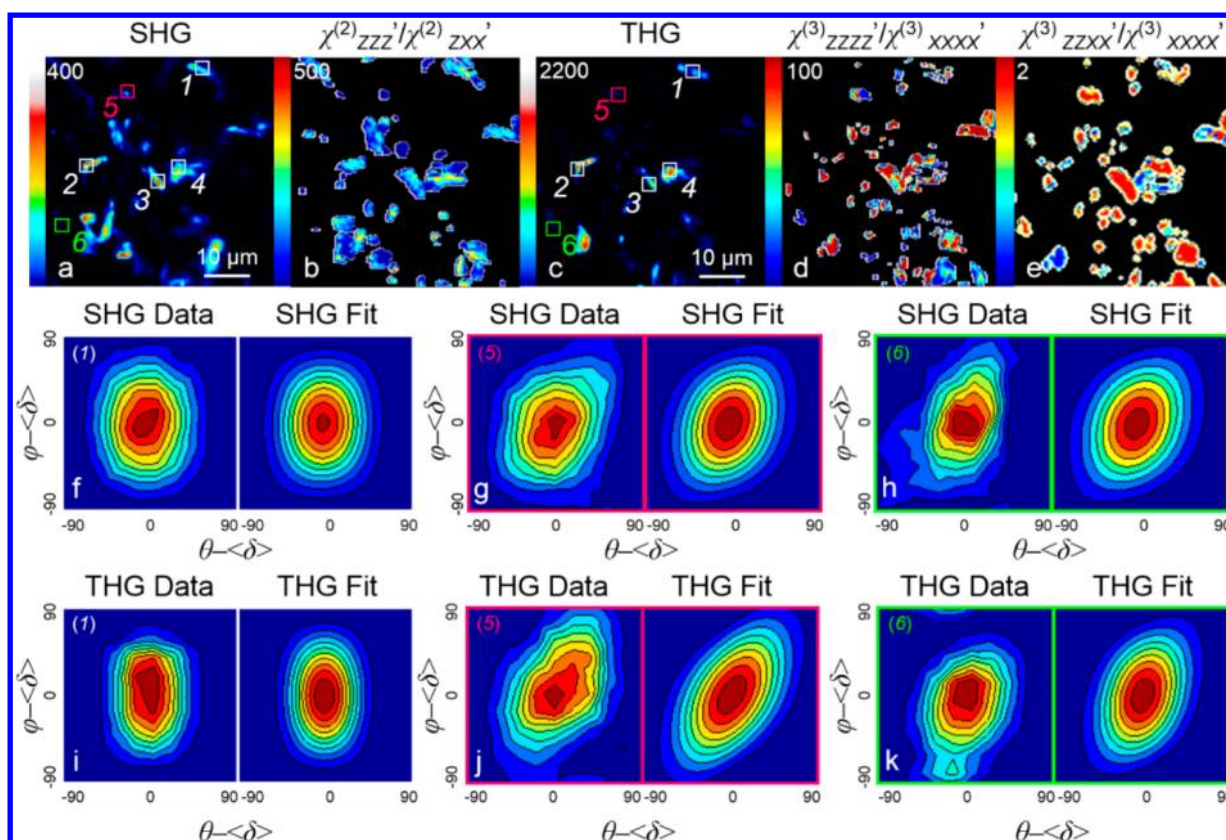dx.doi.org/10.1021/jp411387p | J. Phys. Chem. B 2014, 118, 3814−3822

Figure 2. PIPO plots corresponding to (a) SHG and (c) THG images of crystalline β-carotene aggregates present in orange carrot. (b) The corresponding $\chi^{(2)}_{zzz}{'}/\chi^{(2)}_{zxx}{'}$ values for the SHG image where the color bar ranges from a ratio between 1 and 500 and (d) the corresponding $\chi^{(3)}_{zzzz}{'}/\chi^{(3)}_{xxxx}{'}$ values for the THG image where the color bar ranges from a ratio between 1 and 100; as well as (e) the $\chi^{(3)}_{zzxx}{'}/\chi^{(3)}_{xxxx}{'}$ values where the color bar ranges from a ratio between -2 and 2. (f–k) Different regions (shown in top left corner) were analyzed to produce PIPO data contour plots (left) and fits (right). SHG fits were performed with eq 5 while THG fits were performed with eq 9. The contour plot shown of region *1* is representative of areas of intense SHG and THG signals such as regions *2*, *3*, and *4*, whereas the contour plots representing regions *5* and *6* are typical of areas which do not demonstrate intense SHG and THG signals.

and eq 9 for THG with a Levenberg–Marquardt algorithm. For fitting, $\theta{'}$ and $\varphi{'}$ in eqs 5 and 9 were replaced with $\theta - \langle\delta\rangle$ and $\varphi - \langle\delta\rangle$ where $\langle\delta\rangle$ angle is between the laboratory Z-axis and the projection of the average orientation axis of β-carotene molecules in a pixel onto the XZ image plane.

Fitting of PIPO SHG data was performed analogously to the fitting procedure described elsewhere.[37] Briefly, $\chi^{(2)}_{zzz}{'}$ and $\langle\delta\rangle$ were fit assuming $\chi^{(2)}_{zxx}{'} = 1$ and $\chi^{(2)}_{xxx}{'} = \chi^{(2)}_{xzz}{'} = 0$ where the optimal fitting parameters were determined by the R^2 value. The second step included fitting $\chi^{(2)}_{xxx}{'}$ and $\chi^{(2)}_{xzz}{'}$ to account for asymmetry in the PIPO plot where the fitted values of $\chi^{(2)}_{zzz}{'}$ and $\langle\delta\rangle$ were used as initial parameters with tight bounds. If there was no appreciable improvement in the fitting with $\chi^{(2)}_{xxx}{'}$ and $\chi^{(2)}_{xzz}{'}$ variables set as free parameters, then the results of the initial fit were used. The process was then repeated for each selected area. Similarly, fitting of PIPO THG data was performed by fixing $\chi^{(3)}_{zzxx}{'}/\chi^{(3)}_{xxxx}{'}$ between -2 and 2 and allowing $\chi^{(3)}_{zzzz}{'}/\chi^{(3)}_{xxxx}{'}$ and $\langle\delta\rangle$ to be fit as free parameters. All code was written in MATLAB (MathWorks). Calibration of the polarization orientation in the microscope was performed with collagen from rat tail tendon.[37]

Fluorescence Lifetime Imaging. The femtosecond Yb:KGd(WO$_4$)$_2$ oscillator was also used for excitation in order to characterize fluorescence lifetimes, and discriminate between fluorescence and SHG signals. The fluorescence signal was collected in the forward direction through a bandpass filter of 525 to 630 nm (Semrock) and focused onto a microchannel plate photomultiplier tube (R3809U-50 MCP-PMT, Hamamatsu). Fluorescence images were acquired with a SPC830 card (Becker & Hickl GmbH). The time-correlated single-photon-counting (TCSPC) method was employed for detection.[42]

RESULTS AND DISCUSSION

SHG and THG Images of Carrots. β-Carotene crystalline aggregates in thin slices of orange carrot were imaged simultaneously with SHG and THG microscopy (Figure 1a,b). The β-carotene crystalline aggregates demonstrate high SHG and THG signal intensities where the structures in both images correlate (Figure 1c).

In order to verify that SHG and THG emission was observed from β-carotene crystalline aggregates, the thin slices of orange carrot were submerged in ethanol for 4 h, after which time the carrot tissue became transparent signifying the dissolution of carotenoids. Imaging of the transparent carrot tissue (Figure 1d,e) revealed significantly lower SHG and THG intensities which do not correlate (Figure 1f). The spherical structures observed in the SHG image of the transparent carrot tissue is likely due to starch granules, while in THG, the cell walls can be seen. Therefore, the SHG and THG signals in orange carrot were attributed to the presence of β-carotene crystalline aggregates. Further verification was performed with the TCSPC technique (Supporting Information) which demonstrated that the signal obtained from carrot when using the

SHG filter was comparable to the instrument response time, and thus, the signal was attributed to SHG.

β-Carotene Nonlinear Optical Susceptibilities in Carrot Crystals. PIPO SHG and PIPO THG microscopy was used to investigate the organizational structure of β-carotene crystals in carrot where the data is summarized in Figure 2. The SHG and THG images of β-carotene crystals are presented in panels (a) and (c), respectively. The polarization data for 2 × 2 pixel areas represented by the regions in Figure 2a and c are shown in the left parts of the panels below: f and i representing regions *1* to *4*, g and j for region *5*, and h and k for region *6*. The corresponding fits to the polarization data with eqs 5 and 9 for SHG and THG, respectively, are shown in the right parts of the same panels of Figure 2, f to k.

The typical $\chi^{(2)}_{ZZZ}{}'/\chi^{(2)}_{ZXX}{}'$ ratio for the β-carotene crystals studied in areas of strong SHG signal (Figure 2a regions *1, 2, 3,* and *4*) was found to have good fits ($R^2 > 0.92$) and ratio values above 20 (Table 1) indicating that the polarization of the

Table 1. Summary of Fitting Parameters from PIPO SHG and PIPO THG Data of Crystalline β-Carotene Aggregates Present in Orange Carrot Pertaining to Specific Regions Highlighted in Figure 2[a]

region	$\dfrac{\chi^{(2)}_{ZZZ}{}'}{\chi^{(2)}_{ZXX}{}'}$	$\dfrac{\chi^{(3)}_{ZZZZ}{}'}{\chi^{(3)}_{XXXX}{}'}$	$\dfrac{\chi^{(3)}_{ZZZZ}{}'}{\chi^{(3)}_{ZZXX}{}'}$	$\dfrac{\chi^{(3)}_{ZZXX}{}'}{\chi^{(3)}_{XXXX}{}'}$
1	190 ± 170	27 ± 11	−90 ± 130	−0.3 ± 0.4
2	250 ± 230	42 ± 31	42 ± 35	1 ± 0.4
3	120 ± 110	23 ± 11	23 ± 14	1 ± 0.4
4	220 ± 200	15 ± 6	−50 ± 140	−0.3 ± 0.4
5	3.8 ± 0.8	5 ± 3	5.0 ± 3.6	1 ± 0.4
6	7.5 ± 1.3	7 ± 4	7.0 ± 4.9	1 ± 0.4

[a] R^2 values for SHG fits were at least 0.92 and R^2 values for THG fits were at least 0.93. The $\chi^{(3)}_{ZZXX}{}'/\chi^{(3)}_{XXXX}{}'$ parameter was fixed between −2 and 2, and $\chi^{(3)}_{ZZZZ}{}'/\chi^{(3)}_{XXXX}{}'$ was set as a free fitting parameter.

incident laser along the Z′-axis results mostly in radiation along the Z′-axis, while polarization along the X′-axis results in a comparatively small value for the radiation along the Z′-axis. The large error in these ratios occurs because the fitting of $\chi^{(2)}_{ZZZ}{}'/\chi^{(2)}_{ZXX}{}'$ values above 20 has low sensitivity to the susceptibility ratios. Nevertheless, ratios above 20 signify that the alignment of β-carotene molecules is uniaxial where it is presumed that the dominating molecular nonlinear dipole for trans β-carotene is along the conjugated backbone.[43]

Regions of low SHG signal intensity (Figure 2a regions *5* and *6*) also had good fits ($R^2 > 0.92$), but the $\chi^{(2)}_{ZZZ}{}'/\chi^{(2)}_{ZXX}{}'$ ratio was found to be below 10. The $\chi^{(2)}_{ZZZ}{}'/\chi^{(2)}_{ZXX}{}'$ ratio changes as a result of the orientation of trans β-carotene molecules with respect to the image plane.[36] Therefore, regions of high ratio are indicative of trans β-carotene molecules oriented along the image plane, whereas regions of low ratio are representative of trans β-carotene molecules tilted out of the plane.

Evaluation of the THG PIPO data was performed to obtain complementary structural information about the organization of β-carotene in the aggregates. PIPO THG data was analyzed in the same regions as the PIPO SHG data and revealed similar, albeit different, results as SHG. The fits to the data with eq 9 were good ($R^2 > 0.93$), revealing $\chi^{(3)}_{ZZZZ}{}'/\chi^{(3)}_{XXXX}{}'$ to be large (average $\chi^{(3)}_{ZZZZ}{}'/\chi^{(3)}_{XXXX}{}' = 27 \pm 11$) for regions of intense SHG and THG signal (Figure 2c regions *1, 2, 3,* and *4*). Large $\chi^{(3)}_{ZZZZ}{}'/\chi^{(3)}_{XXXX}{}'$ ratio values indicate radiation polarized along the Z′-axis induced by laser polarization along the Z′-axis is

large, while polarization along the X′-axis results in a small amount of THG radiation polarized along the X′-axis. The second THG fitting parameter for these regions (eq 9), $\chi^{(3)}_{ZZZZ}{}'/\chi^{(3)}_{ZZXX}{}'$, is also large, while the values of $\chi^{(3)}_{ZZXX}{}'/\chi^{(3)}_{XXXX}{}'$ were found to be small. Therefore, similar to the PIPO SHG data, the PIPO THG data revealed that β-carotene molecules are oriented with one dominant nonlinear dipole.

In analogy with the low-intensity SHG and THG signals (Figure 2c regions *5* and *6*), THG had smaller ratio values (average $\chi^{(3)}_{ZZZZ}{}'/\chi^{(3)}_{XXXX}{}' = 6 \pm 3$) as compared to values found in regions of high SHG and THG signal, signifying that the average orientation of trans β-carotene molecules in the focal volume are tilted out of the image plane. The THG data showed similar results to SHG PIPO, verifying that PIPO THG can also be used to determine organization of the structure.

Isolated chromoplasts from carrot were also studied by PIPO SHG and PIPO THG analysis to verify that the polarization dependent data collected in Figure 2 corresponds to crystalline β-carotene aggregates contained in chromoplasts. The isolated chromoplasts demonstrated similar PIPO SHG and PIPO THG plots to that of carrot slices with similar second-order and third-order nonlinear optical susceptibility ratios (data not shown). Therefore, this verifies that the PIPO SHG and PIPO THG data obtained from orange carrot slices corresponds to crystalline β-carotene aggregates in chromoplasts.

Three-Dimensional Orientation of trans β-Carotene Molecules in Carrots. In order to evaluate the organization of β-carotene molecules in crystalline aggregates present in orange carrot, the average orientation of β-carotene molecules within a focal volume was extracted from polarization-dependent SHG (Figure 3a,g) and THG (Figure 3d,j) images, where data only with an R^2 value of 0.8 and greater was considered. Examples of the orientation of β-carotene molecules in crystalline aggregates found in slices of orange carrot are shown in the cylindrical axis projection images in Figure 3b,e,h,k. The projection orientation of β-carotene molecules in crystalline aggregates with respect to their aggregate axis as determined by PIPO SHG and PIPO THG is summarized in Table 2.

The orientation of β-carotene molecules from the aggregate axis varies largely (Table 2). In rare occasions (samples are not shown), the orientation of β-carotene molecules from the aggregate can be as high as 70°; however, in a large number of cases, the β-carotene axis orientation is close to the aggregate axis. The orientation of β-carotene molecules at angles less than 32° is indicative of J-aggregate formation.[1] The absorbance of isolated chromoplasts (Supporting Information) was found to be red-shifted compared to the absorbance of β-carotene dissolved in solvent, which is also indicative of the formation of J-aggregates. Therefore, PIPO SHG and PIPO THG can be used to determine the orientation of β-carotene molecules with respect to the aggregate axis.

According to Frey-Wyssling and Schwegler, trans β-carotene molecules in carrots arrange to form sheets.[7] The growth of sheets in a single direction can cause the formation of narrow ribbons referred to as needles, whereas more broad-like ribbons can elongate and wind into coils forming helical tubes.[7] The reason different angles are observed for the orientation of β-carotene molecules from the aggregate axis is that sheets of β-carotene molecules can be folded in a different way and have a different twist with respect to their projection on the image plane. If multiple sheets that are folded appear in the same focal volume, then β-carotene molecules may be oriented in several directions. Therefore, due to the coherent summation of the
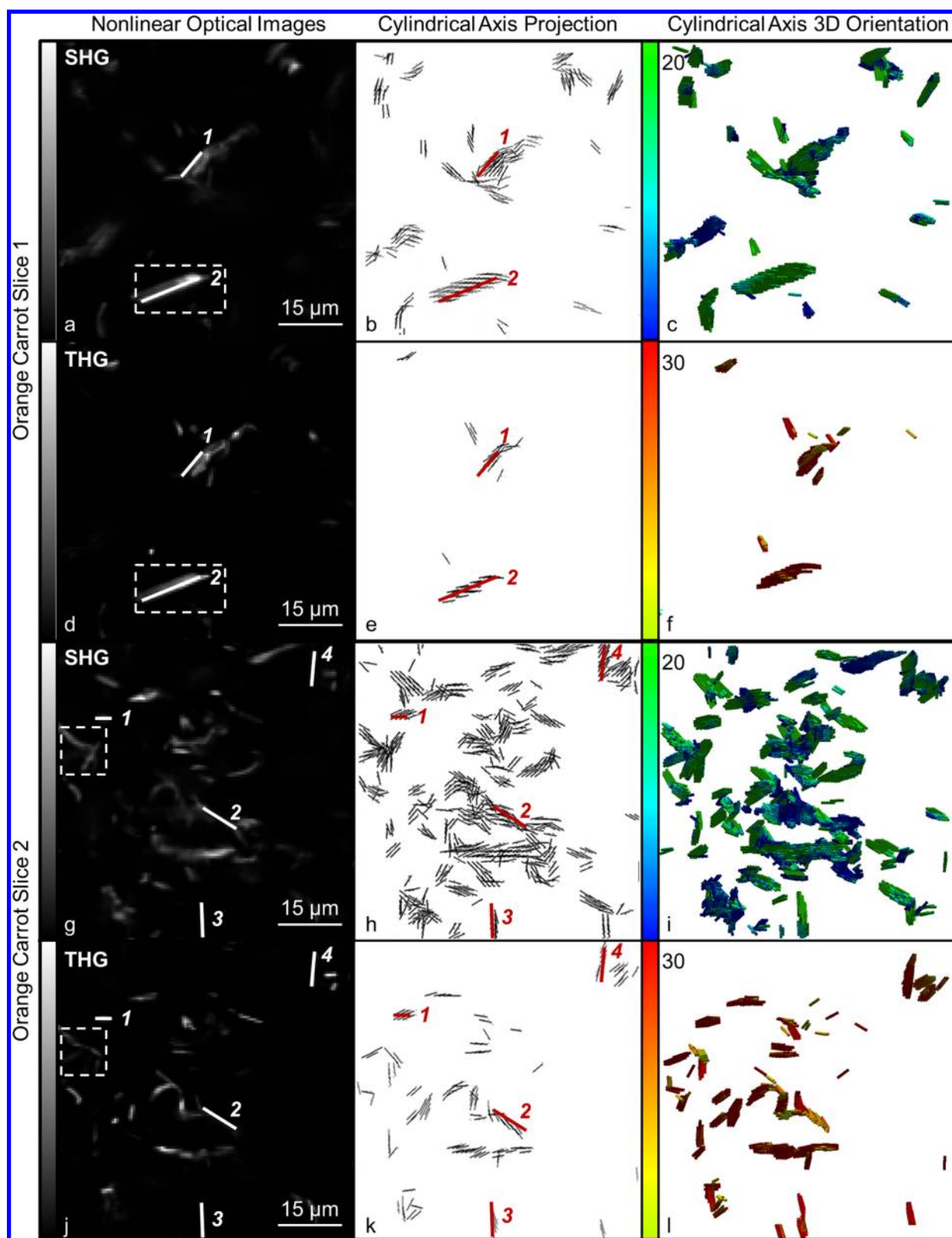
Figure 3. Cylindrical axis projection images and cylindrical axis three-dimensional orientation images representing the average orientation of β-carotene molecules in a focal volume in crystalline aggregates. SHG images (a, g) and the corresponding THG images (d, j) of thin slices of orange carrot containing trans β-carotene crystalline aggregates. A vector image of the average orientation of trans β-carotene molecules in a focal volume is represented for SHG (b,h) and THG (e,k). A three-dimensional representation of the average orientation of trans β-carotene molecules in a focal volume is also shown for SHG (c,i) and THG (f,l). The SHG color bar represents $\chi^{(2)}_{zzz}{}'/\chi^{(2)}_{zxx}{}'$ ratios ranging between 1 and 20 and the THG color bar represents $\chi^{(3)}_{zzzz}{}'/\chi^{(3)}_{xxxx}{}'$ ratios ranging between 1 and 30.

Table 2. Orientation of β-Carotene Molecules in Crystalline Aggregates Found in Slices of Orange Carrot with Respect to Their Aggregate Axis[a]

	region	κ $(\pm 2°)$[b]	
		SHG	THG
Orange Carrot Slice 1 Figure 3 (a, d)	1	13	15
	2	11	10
Orange Carrot Slice 2 Figure 3 (g, j)	1	24	25
	2	21	19
	3	24	25
	4	12	14

[a]The regions correspond to specific aggregates seen in Figure 3. The aggregate projection axis on the XZ plane was determined from SHG (Figure 3a,g) and THG images (Figure 3d,j) while the orientation of β-carotene molecules was determined from their corresponding cylindrical axis projection images for SHG (Figure 3b,h) and THG (Figure 3e,k). [b]Orientation angle, κ, of β-carotene molecules from the aggregate axis (measured in degrees).

nonlinear dipoles at different orientations in the focal volume, the resulting cylindrical axis of the voxel may assume various orientations with respect to the apparent axis of the aggregate.[37,39]

From the cylindrical axis projection images in Figure 3, it is difficult to assess the overall structure of the carrot aggregates; however, a three-dimensional (3D) representation may be constructed from knowledge of the second-order nonlinear optical susceptibility ratio ($\chi^{(2)}_{zzz}{}'/\chi^{(2)}_{zxx}{}'$) by applying eqs 1 and 2, and the third-order nonlinear optical susceptibility ratio ($\chi^{(3)}_{zzzz}{}'/\chi^{(3)}_{xxxx}{}'$) by applying eqs 6 and 8, and extracting the angle α.

The colored scale bar in Figure 3 for the 3D images generated from SHG (Figure 3c,i) and THG (Figure 3f,l) indicate the $\chi^{(2)}_{zzz}{}'/\chi^{(2)}_{zxx}{}'$ ratio and the $\chi^{(3)}_{zzzz}{}'/\chi^{(3)}_{xxxx}{}'$

ratio, respectively, for each voxel where the voxel is represented as a cylinder. For SHG, a maximum $\chi^{(2)}_{zzz}{}'/\chi^{(2)}_{zxx}{}'$ ratio of 20 was chosen as the fitting of $\chi^{(2)}_{zzz}{}'/\chi^{(2)}_{zxx}{}'$ values above 20 has low sensitivity to the susceptibility ratios. For THG, a maximum $\chi^{(3)}_{zzzz}{}'/\chi^{(3)}_{xxxx}{}'$ ratio of 30 was chosen as the highest values of $\chi^{(3)}_{zzzz}{}'/\chi^{(3)}_{xxxx}{}'$ seen in Table 1 was about 30. Voxels with $\chi^{(2)}_{zzz}{}'/\chi^{(2)}_{zxx}{}'$ ratios greater than 20 (green cylinders in Figure 3c,i) and $\chi^{(3)}_{zzzz}{}'/\chi^{(3)}_{xxxx}{}'$ ratios greater than 30 (red cylinders in Figure 3f,l) are oriented in the XZ plane, while $\chi^{(2)}_{zzz}{}'/\chi^{(2)}_{zxx}{}'$ ratios lower than 20 and $\chi^{(3)}_{zzzz}{}'/\chi^{(3)}_{xxxx}{}'$ ratios lower than 30 are tilted out of the XZ plane. Since the equations for $\chi^{(2)}_{zzz}{}'/\chi^{(2)}_{zxx}{}'$ and $\chi^{(3)}_{zzzz}{}'/\chi^{(3)}_{xxxx}{}'$ are even functions, a degeneracy exists between the sign of α, and Figure 3c,f,i,l only demonstrates one possible tilt of the cylindrical axis out of the image plane for each pixel.[37]

A close-up of the 3D orientation of two specific aggregates indicated by a white dashed line box in Figure 3a,d and Figure 3g,j is shown in Figure 4. The correlated 3D images in Figure 4e,f,k,l resemble ribbon structures where there are regions within the aggregate that are lying flat in the XZ plane. Areas within the aggregate where the β-carotene molecules are tilted out of the XZ plane are analogous to the crinkling of a ribbon. In THG, only structures which are in the XZ plane or tilted slightly out of this plane are seen because as the cylindrical structure rotates more out of the XZ plane, the THG signal decreases more rapidly than the SHG signal. This is exemplified in Figure 5 where for SHG (Figure 5a), at half the initial $\chi^{(2)}_{zzz}{}'/\chi^{(2)}_{zxx}{}'$ value, the corresponding α angle reaches about 45°, whereas for THG (Figure 5b), at half the initial $\chi^{(3)}_{zzzz}{}'/\chi^{(3)}_{xxxx}{}'$ value, the angle α reaches only 34°. Thus, if the aggregate structure appears oriented too much out of the image plane, it is no longer observed in THG. Therefore, PIPO SHG reveals a larger range of possible tilt angles.

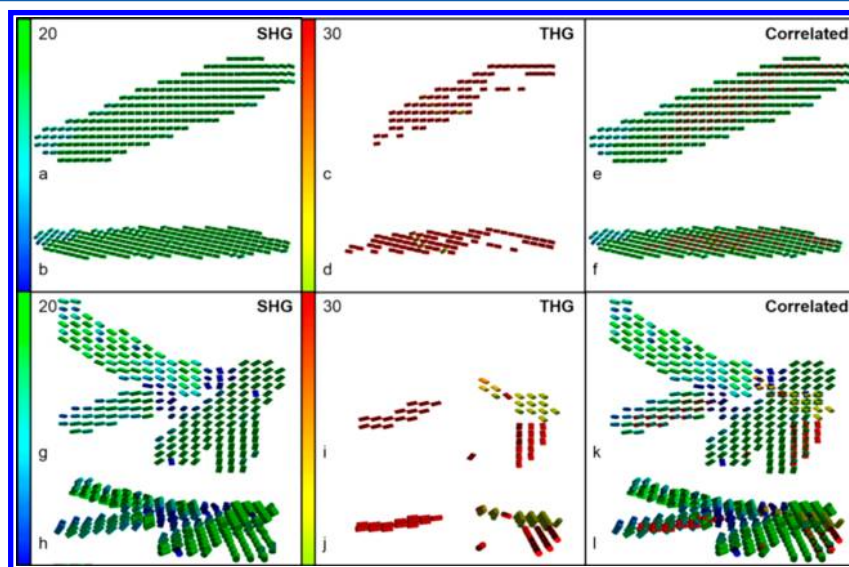For many regions in Figure 4, the 3D representation of the average orientation of trans β-carotene molecules in a focal

Figure 4. Three-dimensional representation of the average orientation of trans β-carotene molecules in a focal volume. Two examples of crystalline β-carotene aggregates were chosen as shown in Figure 3 indicated by white boxes. From analysis of PIPO SHG (a,b,g,h) and PIPO THG (c,d,i,j), the corresponding 3D representation of these two aggregates are shown lying flat (a,c,g,i) and sideways (b,d,i,j). The SHG color bar represents $\chi^{(2)}_{zzz}{}'/\chi^{(2)}_{zxx}{}'$ ratios ranging between 1 and 20 where areas with low $\chi^{(2)}_{zzz}{}'/\chi^{(2)}_{zxx}{}'$ ratios are colored blue and areas of high $\chi^{(2)}_{zzz}{}'/\chi^{(2)}_{zxx}{}'$ ratios are colored green. The THG color bar represents $\chi^{(3)}_{zzzz}{}'/\chi^{(3)}_{xxxx}{}'$ ratios ranging between 1 and 30 where areas with low $\chi^{(3)}_{zzzz}{}'/\chi^{(3)}_{xxxx}{}'$ ratios are colored yellow and areas of high $\chi^{(3)}_{zzzz}{}'/\chi^{(3)}_{xxxx}{}'$ ratios are colored red. Correlated three-dimensional representations are also shown for the aggregate lying flat (e,k) and sideways (f,l).
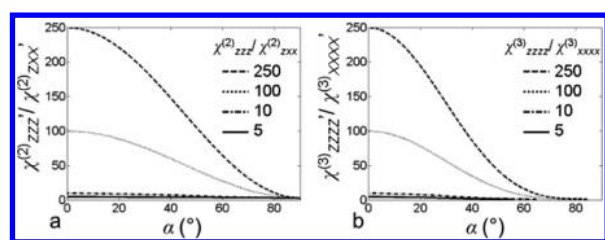
Figure 5. Effect on $\chi^{(2)}_{zzz}{}'/\chi^{(2)}_{zxx}{}'$ (a) and $\chi^{(3)}_{zzzz}{}'/\chi^{(3)}_{xxxx}{}'$ (b) as the angle α changes where α represents the angle between the projection of a β-carotene molecule on the XZ plane. Note that in graph (b), $\chi^{(3)}_{zzxx}{}'/\chi^{(3)}_{xxxx}{}'$ is set to 0. The chosen molecular susceptibility ratio values $\chi^{(2)}_{zzz}/\chi^{(2)}_{zxx}$ and $\chi^{(3)}_{zzzz}/\chi^{(3)}_{xxxx}$ are indicated in the graphs.

volume generated from PIPO SHG data agreed with the 3D representation generated from PIPO THG data where, for example, Figure 4e,f represents a single ribbon mostly aligned along the XZ plane. Regions where deviation in the cylindrical axis orientations from PIPO SHG to PIPO THG data as seen in Figure 4k,l is attributed to regions where the ribbon folds underneath or on top of itself. The presence of several principal directions of dipoles in the focal volume result in an overall cylindrical axis orientation of the voxel, which is different for SHG than THG due to differences in symmetry selection rules for the different order nonlinear susceptibility tensors. The second-order and third-order nonlinear optical susceptibility tensor components describing such a voxel are the result of a coherent summation of the nonlinear dipoles, and hence they are influenced by dipole orientations and affected by radiation phase differences due to the distances between the different layers of the folded ribbon.[44] It has been previously found that asymmetry as determined by a PIPO SHG plot exists for overlapping collagen fibers within the same voxel.[37] However, the signal-to-noise ratio in the crystalline β-carotene aggregate shown in Figure 4g,h was too low to observe asymmetry. This aspect should be investigated to determine whether asymmetry would also occur with PIPO THG. Overall, PIPO SHG and THG microscopy can determine the 3D orientation of harmonophore aggregates inside biological tissues.

CONCLUSIONS

PIPO SHG and PIPO THG microscopy was used to study the orientation of β-carotene molecules within individual aggregates contained in the chromoplasts of orange carrots where PIPO THG microscopy was introduced for the first time. Multimodal PIPO SHG and PIPO THG studies of the aggregates revealed one dominant SHG and THG dipole signifying that the alignment of β-carotene molecules is uniaxial. Further, three-dimensional visualization of the orientation of β-carotene molecules with respect to the aggregate axis was performed and revealed evidence of ribbon-like structures. The small nonlinear dipole orientation angle with respect to the ribbon axis and characteristic red-shift of the absorption peak for β-carotene aggregates are indicative of J-aggregates. In general, both PIPO SHG and PIPO THG microscopy can be applied to reveal structural crystalline parameters and their relative orientation in biological samples *in vivo*, which is important for studying structure–function relationships in biology.

ASSOCIATED CONTENT

⑤ Supporting Information

Theory of PIPO THG, UV–Vis absorption spectra of isolated chromoplasts from orange carrot, and fluorescence lifetime data. This material is available free of charge via the Internet at http://pubs.acs.org.

AUTHOR INFORMATION

Corresponding Author

*Tel.: +1 905 828 3821. Fax: +1 905 828 5425. E-mail: virgis. barzda@utoronto.ca.

Notes

The authors declare no competing financial interest.

ACKNOWLEDGMENTS

ABBREVIATIONS

SHG, second harmonic generation; THG, third harmonic generation; PIPO, polarization-in, polarization-out; 3D, three-dimensional

REFERENCES

(1) Köhn, S.; Kolbe, H.; Korger, M.; Köpsel, C.; Mayer, B.; Auweter, H.; Lüddecke, E.; Bettermann, H.; Martin, H.-D. Aggregation and Interface Behaviour of Carotenoids. In *Carotenoids*; Britton, G., Liaaen-Jensen, S., Pfander., H., Eds.; Birkhäuser: Boston, 2008; Vol. 4, pp 53−98.

(2) Buchwald, M.; Jencks, W. P. Optical Properties of Astaxanthin Solutions and Aggregates. *Biochemistry* **1968**, *7*, 834−843.

(3) Mori, Y.; Yamano, K.; Hashimoto, H. Bistable Aggregate of All-Trans-Astaxanthin in an Aqueous Solution. *Chem. Phys. Lett.* **1996**, *254*, 84−88.

(4) Auweter, H.; Haberkorn, H.; Heckmann, W.; Horn, D.; Luddecke, E.; Rieger, J.; Weiss, H. Supramolecular Structure of Precipitated Nanosize β-Carotene Particles. *Angew. Chem., Int. Ed. Engl.* **1999**, *38*, 2188−2191.

(5) Köpsel, C.; Möltgen, H.; Schuch, H.; Auweter, H.; Kleinermanns, K.; Martin, H. D.; Bettermann, H. Structure Investigations on Assembled Astaxanthin Molecules. *J. Mol. Struct.* **2005**, *750*, 109−115.

(6) Giovannetti, R.; Alibabaei, L.; Pucciarelli, F. Kinetic Model for Astaxanthin Aggregation in Water-Methanol Mixtures. *Spectrochim. Acta, Part A* **2009**, *73*, 157−162.

(7) Frey-Wyssling, A.; Schwegler, F. Ultrastructure of Chromoplasts in Carrot Root. *J. Ultrastruct. Res.* **1965**, *13*, 543−559.

(8) Grote, M.; Fromme, H. G. Electron Microscopic Studies in Cultivated Plants. II. Fresh and Stored Roots of *Daucus carota* L. *Z. Lebensm. Unters. Forsch.* **1978**, *166*, 74−79.

(9) Kim, J. E.; Rensing, K. H.; Douglas, C. J.; Cheng, K. M. Chromoplasts Ultrastructure and Estimated Carotene Content in Root Secondary Phloem of Different Carrot Varieties. *Planta* **2010**, *231*, 549−558.

(10) Ben-Shaul, Y.; Naftali, Y. The Development and Ultrastructure of Lycopene Bodies in Chromoplasts of *Lycopersicum esculentum*. *Protoplasma* **1969**, *67*, 333−344.

(11) Ben-Shaul, Y.; Klein, S. Development and Structure of Carotene Bodies in Carrot Roots. *Bot. Gaz.* **1965**, *126*, 79−85.

(12) Brackmann, C.; Bengtsson, A.; Alminger, M. L.; Svanberg, U.; Enejder, A. Visualization of β-carotene and Starch Granules in Plant Cells Using CARS and SHG Microscopy. *J. Raman Spectrosc.* **2011**, *42*, 586−592.

(13) Brown, E.; McKee, T.; diTomaso, E.; Pluen, A.; Seed, B.; Boucher, Y.; Jain, R. K. Dynamic Imaging of Collagen and its

Modulation in Tumors *in vivo* Using Second-Harmonic Generation. *Nat. Med.* **2003**, *9*, 796−800.

(14) Stoller, P.; Kim, B. M.; Rubenchik, A. M.; Reiser, K. M.; Da Silva, L. B. Polarization-Dependent Optical Second-Harmonic Imaging of a Rat-Tail Tendon. *J. Biomed. Opt.* **2002**, *7*, 205−214.

(15) Stoller, P.; Reiser, K. M.; Celliers, P. M.; Rubenchik, A. M. Polarization-Modulated Second Harmonic Generation in Collagen. *Biophys. J.* **2002**, *82*, 3330−3342.

(16) Stoller, P.; Celliers, P. M.; Reiser, K. M.; Rubenchik, A. M. Quantitative Second-Harmonic Generation Microscopy in Collagen. *Appl. Opt.* **2003**, *42*, 5209−5219.

(17) Freund, I.; Deutsch, M.; Sprecher, A. Connective Tissue Polarity. Optical Second-Harmonic Microscopy, Crossed-Beam Summation, and Small-Angle Scattering in Rat-Tail Tendon. *Biophys. J.* **1986**, *50*, 693−712.

(18) Chen, X. Y.; Nadiarynkh, O.; Plotnikov, S.; Campagnola, P. J. Second Harmonic Generation Microscopy for Quantitative Analysis of Collagen Fibrillar Structure. *Nat. Protoc.* **2012**, *7*, 654−669.

(19) Williams, R. M.; Zipfel, W. R.; Webb, W. W. Interpreting Second-Harmonic Generation Images of Collagen I Fibrils. *Biophys. J.* **2005**, *88*, 1377−1386.

(20) Roth, S.; Freund, I. Second Harmonic Generation in Collagen. *J. Chem. Phys.* **1979**, *70*, 1637−1643.

(21) Tiaho, F.; Recher, G.; Rouede, D. Estimation of Helical Angles of Myosin and Collagen by Second Harmonic Generation Imaging Microscopy. *Opt. Express* **2007**, *15*, 12286−12295.

(22) Schurmann, S.; von Wegner, F.; Fink, R. H. A.; Friedrich, O.; Vogel, M. Second Harmonic Generation Microscopy Probes Different States of Motor Protein Interaction in Myofibrils. *Biophys. J.* **2010**, *99*, 1842−1851.

(23) Chu, S. W.; Chen, S. Y.; Chern, G. W.; Tsai, T. H.; Chen, Y. C.; Lin, B. L.; Sun, C. K. Studies of $\chi(2)/\chi(3)$ Tensors in Submicron-Scaled Bio-Tissues by Polarization Harmonics Optical Microscopy. *Biophys. J.* **2004**, *86*, 3914−3922.

(24) Psilodimitrakopoulos, S.; Santos, S. I. C. O.; Amat-Roldan, I.; Thayil, A. K. N.; Artigas, D.; Loza-Alvarez, P. In vivo, Pixel-Resolution Mapping of Thick Filaments' Orientation in Nonfibrilar Muscle Using Polarization-Sensitive Second Harmonic Generation Microscopy. *J. Biomed. Opt.* **2009**, *14*, 0140011−01400111.

(25) Chou, C. K.; Chen, W. L.; Fwu, P. T.; Lin, S. J.; Lee, H. S.; Dong, C. Y. Polarization Ellipticity Compensation in Polarization Second-Harmonic Generation Microscopy without Specimen Rotation. *J. Biomed. Opt.* **2008**, *13*, 0140051−0140057.

(26) Plotnikov, S. V.; Millard, A. C.; Campagnola, P. J.; Mohler, W. A. Characterization of the Myosin-Based Source for Second-Harmonic Generation from Muscle Sarcomeres. *Biophys. J.* **2006**, *90*, 693−703.

(27) Nucciotti, V.; Stringari, C.; Sacconi, L.; Vanzi, F.; Fusi, L.; Linari, M.; Piazzesi, G.; Lombardi, V.; Pavone, F. S. Probing Myosin Structural Conformation in vivo by Second-Harmonic Generation Microscopy. *Proc. Natl. Acad. Sci. U.S.A.* **2010**, *107*, 7763−7768.

(28) Psilodimitrakopoulos, S.; Petegnief, V.; de Vera, N.; Hernandez, O.; Artigas, D.; Planas, A. M.; Loza-Alvarez, P. Quantitative Imaging of Microtubule Alteration as an Early Marker of Axonal Degeneration After Ischemia in Neurons. *Biophys. J.* **2013**, *104*, 968−975.

(29) Dombeck, D. A.; Kasischke, K. A.; Vishwasrao, H. D.; Ingelsson, M.; Hyman, B. T.; Webb, W. W. Uniform Polarity Microtubule Assemblies Imaged in Native Brain Tissue by Second-Harmonic Generation Microscopy. *Proc. Natl. Acad. Sci. U.S.A.* **2003**, *100*, 7081−7086.

(30) Cisek, R.; Prent, N.; Greenhalgh, C.; Sandkuijl, D.; Tuer, A.; Major, A.; Barzda, V. Multicontrast nonlinear imaging microscopy. In *Biochemical applications of nonlinear optical spectroscopy*; Yakovlev, V. V., Ed.; CRC Press: New York, 2009; pp 71−102.

(31) Psilodimitrakopoulos, S.; Amat-Roldan, I.; Loza-Alvarez, P.; Artigas, D. Estimating the Helical Pitch Angle of Amylopectin in Starch Using Polarization Second Harmonic Generation Microscopy. *J. Opt.* **2010**, *12*, 0840071−0840076.

(32) Mazumder, N.; Qiu, J. J.; Foreman, M. R.; Romero, C. M.; Torok, P.; Kao, F. J. Stokes Vector Based Polarization Resolved Second Harmonic Microscopy of Starch Granules. *Biomed. Opt. Express* **2013**, *4*, 538−547.

(33) DeWalt, E. L.; Begue, V. J.; Ronau, J. A.; Sullivan, S. Z.; Das, C.; Simpson, G. J. Polarization-Resolved Second-Harmonic Generation Microscopy as a Method to Visualize Protein-Crystal Domains. *Acta Crystallogr., Sect. D: Biol. Crystallogr.* **2013**, *69*, 74−81.

(34) Olivier, N.; Aptel, F.; Plamann, K.; Schanne-Klein, M. C.; Beaurepaire, E. Harmonic Microscopy of Isotropic and Anisotropic Microstructure of the Human Cornea. *Opt. Express* **2010**, *18*, 5028−5040.

(35) Zimmerley, M.; Mahou, P.; Debarre, D.; Schanne-Klein, M. C.; Beaurepaire, E. Probing Ordered Lipid Assemblies with Polarized Third-Harmonic-Generation Microscopy. *Phys. Rev. X* **2013**, *3*, 0110021−01100216.

(36) Tuer, A. E.; Krouglov, S.; Prent, N.; Cisek, R.; Sandkuijl, D.; Yasufuku, K.; Wilson, B. C.; Barzda, V. Nonlinear Optical Properties of Type I Collagen Fibers Studied by Polarization Dependent Second Harmonic Generation Microscopy. *J. Phys. Chem. B* **2011**, *115*, 12759−12769.

(37) Tuer, A. E.; Akens, M. K.; Krouglov, S.; Sandkuijl, D.; Wilson, B. C.; Whyne, C. M.; Barzda, V. Hierarchical Model of Fibrillar Collagen Organization for Interpreting the Second-Order Susceptibility Tensors in Biological Tissue. *Biophys. J.* **2012**, *103*, 2093−2105.

(38) Dick, B. Irreducible Tensor Analysis of Sum-Frequency and Difference-Frequency-Generation in Partially Oriented Samples. *Chem. Phys.* **1985**, *96*, 199−215.

(39) Garab, G.; Faludi-Daniel, A.; Sutherland, J. C.; Hind, G. Macroorganization of Chlorophyll a/b Light-Harvesting Complex in Thylakoids and Aggregates: Information from Circular Differential Scattering. *Biochemistry* **1988**, *27*, 2425−2430.

(40) Major, A.; Cisek, R.; Sandkuijl, D.; Barzda, V. Femtosecond Yb:KGd(WO$_4$)$_2$ Laser with > 100 nJ of Pulse Energy. *Laser Phys. Lett.* **2009**, *6*, 272−274.

(41) Greenhalgh, C.; Prent, N.; Green, C.; Cisek, R.; Major, A.; Stewart, B.; Barzda, V. Influence of Semicrystalline Order on the Second-Harmonic Generation Efficiency in the Anisotropic Bands of Myocytes. *Appl. Opt.* **2007**, *46*, 1852−1859.

(42) Becker, W. *The bh TCSPC Handbook*, 3rd ed.; Becker & Hickl GmbH: Berlin, 2008.

(43) van Beek, J. B.; Kajzar, F.; Albrecht, A. C. Resonant Third-Harmonic Generation in All-Trans β-carotene: The Vibronic Origins of the Third-Order Nonlinear Susceptibility in the Visible Region. *J. Chem. Phys.* **1991**, *95*, 6400−6412.

(44) Sandkuijl, D.; Tuer, A. E.; Tokarz, D.; Sipe, J. E.; Barzda, V. Numerical Second- and Third-Harmonic Generation Microscopy. *J. Opt. Soc. Am. B* **2013**, *30*, 382−395.

3822

dx.doi.org/10.1021/jp411387p | *J. Phys. Chem. B* 2014, 118, 3814−3822